

Profiles of dark haloes: evolution, scatter, and environment

J. S. Bullock¹, T. S. Kolatt^{1,2}, Y. Sigad², R.S. Somerville², A. V. Kravtsov³,
A. A. Klypin³, J. R. Primack¹, and A. Dekel²

¹*Physics Department, University of California, Santa Cruz, CA 95064 USA*

²*Racah Institute of Physics, The Hebrew University, Jerusalem*

³*Astronomy Department, New Mexico State University, Box 30001, Dept. 4500, Las Cruces, NM 88003-0001 USA*

21 February 2019

ABSTRACT

We study dark-matter halo density profiles in a high-resolution N-body simulation of a Λ CDM cosmology. Our statistical sample contains ~ 5000 haloes in the range $10^{11} - 10^{14} h^{-1} M_{\odot}$ and the resolution allows a study of subhaloes inside host haloes. The profiles are parameterized by an NFW form with two parameters, an inner radius r_s and a virial radius R_{vir} , and we define the halo concentration $c_{\text{vir}} \equiv R_{\text{vir}}/r_s$. First, we find that, for a given halo mass, the redshift dependence of the median concentration is $c_{\text{vir}} \propto (1+z)^{-1}$. This corresponds to $r_s(z) \sim \text{constant}$, and is contrary to earlier suspicions that c_{vir} does not vary much with redshift. The implications are that high-redshift galaxies are predicted to be more extended and dimmer than expected before. Second, we find that the scatter in halo profiles is large, with a 1σ $\Delta(\log c_{\text{vir}}) = 0.18$ at a given mass, corresponding to a scatter in maximum rotation velocities of $\Delta V_{\text{max}}/V_{\text{max}} = 0.12$. We discuss implications for modelling the Tully-Fisher relation, which has a smaller reported intrinsic scatter. Third, subhaloes and haloes in dense environments tend to be more concentrated than isolated haloes, and show a larger scatter. These results suggest that c_{vir} is an essential parameter for the theory of galaxy modelling, and we briefly discuss implications for the universality of the Tully-Fisher relation, the formation of low surface brightness galaxies, and the origin of the Hubble sequence. We present an improved analytic treatment of halo formation that fits the measured relations between halo parameters and their redshift dependence, and can thus serve semi-analytic studies of galaxy formation.

Key words: cosmology — dark matter — galaxies: formation — galaxies: structure

1 INTRODUCTION

In the “standard” picture of galaxy formation, dark-matter (DM) haloes provide the framework for the formation of luminous galaxies (e.g., White & Rees 1978; Blumenthal et al. 1984; White & Frenk 1991). The DM haloes are assumed to form hierarchically bottom-up via gravitational amplification of initial density fluctuations. The haloes carry with them gas, which eventually cools and contracts to form luminous disc galaxies at the halo centres. The halo profile has a direct dynamical role in determining the observable rotation curve of the disc. It also affects gas cooling and infall and therefore the structural properties of the resultant disc, such as size, luminosity and surface brightness. In order to model properly the dissipative stages of galaxy formation and obtain meaningful predictions for observable quantities (such as the Tully-Fisher relation), it is important to perform detailed dynamical studies of the evolution of halo structure, and to obtain statistical characteristics based on a fair sample of the simulated halo population.

Most naturally, the density profiles of haloes are expected to be a two-parameter family. This is because, assuming that the formation of haloes can be approximated by spherical collapse, each proto-halo perturbation can be characterized by two quantities, e.g., mass and radius (or density contrast) at some fiducial cosmological time. In the approximation of spherical collapse, these parameters specify the full evolution of each halo, including the epoch at which it collapses and its virial radius. A successful two-parameter functional form for the halo profiles has been proposed by Navarro, Frenk, & White (1995, 1996, 1997, hereafter NFW95, NFW96, and NFW97):

$$\rho_{\text{NFW}}(r) = \frac{\rho_s}{(r/r_s)(1+r/r_s)^2}, \quad (1)$$

where r_s is a characteristic “inner” radius, and ρ_s a corresponding inner density. As we show in § 2, one of the inner parameters can be replaced by a “virial” parameter, either the virial radius (R_{vir}), mass (M_{vir}), or velocity (V_{vir}). A very useful alternative is the concentration parameter c_{vir} ,

which relates the inner and virial parameters. NFW found that this functional form provides a good fit to haloes over a large range of masses, and for several different cosmological scenarios. It has been tested for the Einstein-deSitter model with a standard CDM power spectrum of initial fluctuations (SCDM), a flat cosmological model with $\Omega_m = 0.3$, $\Omega_\Lambda = 0.7$ and a corresponding CDM power spectrum (Λ CDM), and several models with power-law power spectra (confirmed by Craig 1997, and Kravtsov, Klypin, & Khokhlov 1997, hereafter KKK97).

NFW then noticed that, for a given cosmology, their haloes show a strong correlation between the model's two parameters, e.g., an increase in ρ_s for decreasing M_{vir} . A natural reason for the fact that low-mass haloes tend to show higher densities is that they typically collapsed earlier, when the universe was denser. To model this trend, NFW proposed a toy model (outlined in Appendix A) which assumes that ρ_s is a constant multiple k of the universal density $\rho_u(z_c)$ at a collapse redshift z_c , and that the collapsing mass at z_c is a constant fraction f of the total halo mass that has just collapsed and virialized at $z = 0$. The general trend of the relation between the two profile parameters at $z = 0$ is reproduced well for a proper choice of values for the constants k and f , with different values for the different cosmological models.

Since the halo profiles are expected to be a two-parameter family, it is important to study the scatter about this mean relation between the two halo parameters. This scatter could provide the second parameter which is necessary in order to explain the observed variations in galaxy properties, such as bulge-to-disc ratio, size and surface brightness. It may be argued that the scatter in halo spin parameter may also contribute to these variations, but it cannot account for all of them because, e.g., it does not properly correlate with the environment. The scatter in halo profiles should also have direct implications for understanding the surprisingly tight scatter observed in the Tully-Fisher (TF) relation for disc galaxies. NFW found a small scatter among their simulated haloes, which could have provided a convenient explanation for the small TF scatter, but other theoretical studies predict a larger scatter (Eisenstein & Loeb 1996), and the generality of the NFW result is limited by the small number of haloes simulated per cosmology (~ 20) and by their selective choice of haloes near virial equilibrium. We therefore here set to study in detail the scatter in a large, “fair” sample of simulated haloes.

The accumulating data of galaxies at high redshifts provide a great incentive for studying the properties of the halo population as a function of redshift. NFW97 tried to extend their toy model in order to predict this redshift dependence by assuming that k and f are both constant in time. In order to actually study in detail the redshift dependence of halo profiles, we use our large statistical sample of simulated haloes. Our results below, which differ from the NFW97 toy-model predictions at $z \geq 1$, motivate modifications in the toy model in order to properly account for the simulated behavior.

We present here an analysis of a statistical sample of halo profiles drawn from cosmological N-body simulations of Λ CDM with $\Omega_m = 0.3$ and $\Omega_\Lambda = 0.7$. The unprecedented features of this analysis are:

- The sample is large, containing about 5000 haloes in the mass range $10^{11} - 10^{14} h^{-1} M_\odot$ at $z = 0$.
- The sampling is “fair”, in the sense that haloes are found in any environment, field and clustered, and irrespective of the dynamical stage of the halo after virialization.
- The resolution is high, allowing a distinction between “distinct” haloes and “subhaloes”, and a study of environmental trends.
- The time evolution and scatter about the one-parameter family are studied in detail.

In § 2 we discuss further the parametric functional form used for the halo profiles. In § 3 we present the revised toy model for predicting the mean relation between the halo profile parameters and its redshift dependence. In § 4 we describe our N-body simulations and our method of halo finding and classification. In § 5 we present our results for haloes at $z = 0$; we compare the mean result to our model prediction, and quantify the intrinsic scatter. In § 6 we discuss implications for observable rotation curves and the TF relation. In § 7 we investigate the redshift dependence of halo properties, and the toy-model fits. Finally, in § 8, we summarize our results and discuss further implications.

2 PROFILE CHARACTERISTICS

We choose to fit the density profiles of all haloes at all redshifts with the NFW two-parameter functional form (Eq. 1). This is a convenient way to parameterize the profiles, without implying that it necessarily provides the best possible fit. Indeed, a similar analysis could be carried out using alternative functional forms (see an example below). In this section, we discuss the various parameters that are associated with the halo density profile, and the relations between them.

The inner radius, r_s , is where the effective logarithmic slope of the profile is -2 , a characteristic radius which we term r_{-2} . For much smaller radii, $\rho_{\text{NFW}} \propto r^{-1}$, and for much larger radii, $\rho_{\text{NFW}} \propto r^{-3}$. The inner density parameter of the NFW profile is related to the NFW density at r_s by $\rho_s = 4\rho_{\text{NFW}}(r_s)$, and equals the local density at about half r_s : $\rho_s = \rho_{\text{NFW}}(r = 0.466 r_s)$.

The outer, virial radius R_{vir} , of a halo of virial mass M_{vir} , is defined as the radius within which the mean density is Δ_{vir} times the mean universal density ρ_u at that redshift: *

$$M_{\text{vir}} \equiv \frac{4\pi}{3} \Delta_{\text{vir}} \rho_u R_{\text{vir}}^3. \quad (2)$$

The associated virial velocity is defined by[†] $V_{\text{vir}}^2 \equiv GM_{\text{vir}}/R_{\text{vir}}$. The one-to-one relations between the three virial parameters are fully determined by the background cosmology (independent of the inner halo structure), so only one of them at a time can serve in the pair of independent parameters characterizing the profile. The virial overdensity Δ_{vir} is provided by the dissipationless spherical top-hat

*

$M_{\text{vir}} \simeq 10^{11} h^{-1} M_\odot (\Omega_0 \Delta_{\text{vir}}(z)/200) [R_{\text{vir}}(1+z)/75 h^{-1} \text{kpc}]^3$.
[†] $V_{\text{vir}} \simeq 75 \text{km/s} (R_{\text{vir}}/75 h^{-1} \text{kpc}) (\Omega_0 \Delta_{\text{vir}}(z)/200)^{1/3} (1+z)^{3/2}$.

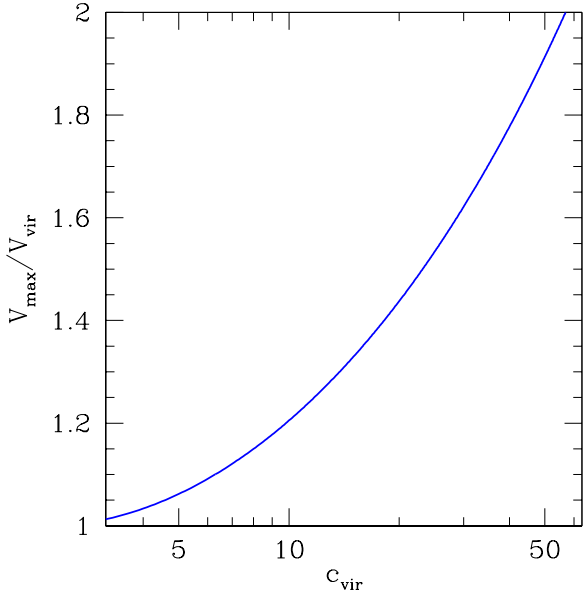


Figure 1. Maximum velocity versus concentration. The maximum rotation velocity for an NFW halo in units of the rotation velocity at its virial radius as a function of halo concentration.

collapse model (Peebles 1984); it is a function of the cosmological model, and it may vary with time. For the Einstein-deSitter cosmology, the familiar value is $\Delta_{\text{vir}} \simeq 200$ at all times. For the family of flat cosmologies ($\Omega_m + \Omega_\Lambda = 1$), the value of Δ_{vir} can be approximated by (Bryan & Norman 1997) $\Delta_{\text{vir}} \simeq (18\pi^2 + 82x - 39x^2)/\Omega(z)$, where $x \equiv \Omega(z) - 1$, and $\Omega(z)$ is the ratio of mean matter density to critical density at redshift z . For example, in the Λ CDM cosmological model that serves as the basis for our analysis in this paper ($\Omega_m = 0.3$), the value at $z = 0$ is $\Delta_{\text{vir}} \simeq 340$.

An associated useful characteristic is the concentration parameter, c_{vir} , defined as the ratio between the virial and inner radii,

$$c_{\text{vir}} \equiv R_{\text{vir}}/r_s. \quad (3)$$

Note that our definition of c_{vir} differs slightly from that originally used by NFW, $c_{\text{NFW}} \equiv R_{200}/r_s$, where R_{200} is the radius corresponding to a density of 200 times the critical density, independent of the actual cosmological model.[‡]

A third relation between the parameters of the NFW profile is

$$M_{\text{vir}} = 4\pi\rho_s r_s^3 A(c_{\text{vir}}), \quad A(c_{\text{vir}}) \equiv \ln(1 + c_{\text{vir}}) - \frac{c_{\text{vir}}}{1 + c_{\text{vir}}}. \quad (4)$$

The three relations (Eqs. 2, 3 and 4) allow the usage of any pair out of the parameters defined so far (excluding degenerate pairs consisting only of virial quantities) as the two independent parameters that fully characterize the profile.

Since the more observable quantities have to do with rotation curves, it is worth translating the density profile into a circular velocity curve for the halo,

[‡] Our definition reduces confusion associated with comparing concentrations of haloes in different cosmologies. For example, when taking into account the model dependence of Δ_{vir} , one realizes that the lower values of c_{NFW} reported by NFW97 for Λ CDM relative to SCDM mainly reflect a difference in virial radii (KKK97).

$$V_c^2(r) \equiv \frac{GM(r)}{r} = V_{\text{vir}}^2 \frac{c_{\text{vir}}}{A(c_{\text{vir}})} \frac{A(x)}{x}, \quad (5)$$

where $x \equiv r/r_s$. The maximum velocity occurs at a radius $r_{\text{max}} \simeq 2.16 r_s$ and is given by

$$\frac{V_{\text{max}}^2}{V_{\text{vir}}^2} \simeq 0.216 \frac{c_{\text{vir}}}{A(c_{\text{vir}})}. \quad (6)$$

For typical c_{vir} values in the range 5–30, V_{max} varies in the range $(1 - 1.6)V_{\text{vir}}$. Figure 1 shows the ratio $V_{\text{max}}/V_{\text{vir}}$ as a function of c_{vir} . Note that for haloes of the same mass, a larger c_{vir} goes with a larger V_{max} . Because of the relationship between r_{max} and r_s , haloes with $c_{\text{vir}} \lesssim 10$ have velocity curves which continue to rise gradually out to an appreciable fraction of their virial radii, while those with $c_{\text{vir}} \gtrsim 10$ rise more steeply, and possibly represent galaxies in which r_{max} is identifiable observationally (though the effects of baryonic contraction should be taken into account before the observed and simulated values of r_{max} can be compared).

We stress again that the specific choice of the NFW functional form does not limit the generality of our analysis in a severe way. This is largely due to the association of the specific r_s with the more general r_{-2} . When the NFW function is fitted to a generic halo whose profile even vaguely resembles a similar shape, the fitting procedure is likely to return an r_s value that is close to the effective r_{-2} of that halo. The concentration parameter can then be interpreted as a general structure parameter not necessarily restricted to the specific NFW function. In particular, any spread in c_{vir} can be attributed to a real scatter in a “physical” inner radius such as r_{-2} rather than to inaccuracies in the assumed universal profile.

The interpretation of r_s as r_{-2} allows one to map the NFW parameters to appropriate parameters of other functional forms. For many purposes, such as determining V_{max} or modelling gas cooling and galaxy formation, the NFW form is sufficiently accurate. However, a comparison with alternative profiles with different core behaviors may be important when much smaller radii are concerned ($r \lesssim 0.02R_{\text{vir}}$), where there are indications of deviations from an extrapolation of the NFW shape (Kravtsov et al. 1998, hereafter KKBP; Primack et al. 1998; Moore et al. 1999).

A specific example of an alternative profile functional form is the Burkert profile (1995):

$$\rho_B(r) = \frac{\rho_b}{[1 + (r/r_b)^2][1 + r/r_b]}. \quad (7)$$

This profile resembles the NFW profile for $r \gtrsim 0.02R_{\text{vir}}$, is similar to the best-fit profile of KKBP at all radii, and seems to do well in fitting haloes from very high resolution N-body simulations (Primack et al. 1998). The Burkert profile has a log slope of -2 at $r_{-2} \simeq 1.52 r_b$, so one can relate the scale radii of NFW and Burkert by $r_b \simeq r_s/1.52$, and then relate the concentration parameters by $R_{\text{vir}}/r_b \simeq 1.52 c_{\text{vir}}$.

Note also that the relationship between c_{vir} and r_{max} is robust, regardless of profile shape. For example, with the Burkert profile we have an implied velocity maximum at $r_{\text{max}} \simeq 3.25 r_b$. If one assumes instead the relation as gleaned from an NFW fit, with $r_{\text{max}} \simeq 2.16 r_s \simeq 3.28 r_b$, there is good agreement between the values of r_{max} .

3 A REVISED TOY MODEL

In any investigation based on computer simulations it is useful to have a simple toy model that helps interpret the numerical results and allows an easy application of the conclusions in subsequent analytic or semi-analytic investigations. As mentioned in the Introduction and outlined in Appendix A, NFW96 and NFW97 proposed such a model, with 2 free parameters, which successfully recovers the mean $c_{\text{vir}}\text{-}M_{\text{vir}}$ relation at $z = 0$ for the several different cosmological models simulated by them. Our simulations (see §5 below) indeed confirm the success of this model at $z = 0$. However, we find (§ 7 below) that the NFW97 model does not reproduce properly the redshift dependence of the halo profiles as seen in the simulation; it significantly over-predicts the concentration of haloes at early times, $z \gtrsim 1$. We therefore propose a revised toy model that is shown below to recover properly the full behavior of the mean $c_{\text{vir}}\text{-}M_{\text{vir}}$ relation and its redshift dependence. We present the model in this preparatory section, so that we can refer to it when we describe and interpret the results from the simulations in the following sections.

3.1 The model

We seek a model for the typical halo concentration, denoted in this section by $c_{\text{vir}}(M_{\text{vir}}, a)$, for a given mass M_{vir} and epoch $a = (1 + z)^{-1}$. Following the general spirit of the NFW97 model, we assign to each halo an epoch of collapse, a_c . Unlike their formulation, which utilizes the extended Press-Schechter approximation, we define a_c in a simpler way as the epoch at which the typical collapsing mass, $M_*(a_c)$, equals a fixed fraction F of the halo mass at epoch a ,

$$M_*(a_c) \equiv FM_{\text{vir}}. \quad (8)$$

The typical collapsing mass at an epoch a is defined by $\sigma[M_*(a)] = 1.686$, where $\sigma(M)$ is the linear rms density fluctuation on the comoving scale encompassing a mass M , and 1.686 is the linear equivalent of the density at collapse according to the familiar spherical collapse model. The typical collapsing mass is therefore a known function of the linear power spectrum of fluctuations and the linear growth rate $D(a)$ for the cosmology in hand. For some purposes we find it convenient to measure the halo mass in units of the typical halo mass at the same epoch,

$$\mu \equiv M_{\text{vir}}(a)/M_*(a). \quad (9)$$

The second relation of the model arises by associating the mean density of the universe ρ_u at a_c with a characteristic density of the halo at a . NFW97 used the inner density parameter ρ_s , which is related to M_{vir} and r_s via the specific shape of the NFW profile. Instead, we define a more general characteristic density $\tilde{\rho}_s$ by combining inner and virial quantities:

$$M_{\text{vir}} \equiv \frac{4\pi}{3} r_s^3 \tilde{\rho}_s. \quad (10)$$

The NFW profile implies $\tilde{\rho}_s = 3\rho_s A(c_{\text{vir}})$. The association of the halo density $\tilde{\rho}_s$ with the universal density at collapse is made via a second free parameter, K :

$$\tilde{\rho}_s = K^3 \Delta_{\text{vir}}(a) \rho_u(a_c) = K^3 \Delta_{\text{vir}}(a) \rho_u(a) \left(\frac{a}{a_c}\right)^3. \quad (11)$$

The parameter K represents contraction of the inner halo beyond that required for top-hat dissipationless halo virialization, and it is assumed to be the same for all haloes. Using Eqs. 2, 10, and 11, we obtain a simple expression for c_{vir} in terms of a_c as our second model relation:

$$c_{\text{vir}}(\mu, a) = K \frac{a}{a_c}. \quad (12)$$

The model is fully determined by Eqs. 8 and 12 given the values of the two parameters F and K . We find below (§ 5 and § 7) that by adjusting F and K we are able to reproduce the full behavior of $c_{\text{vir}}(\mu, a)$ as measured in our simulations. The small differences in the definitions of F and K compared to the analogous parameters of NFW97, f and k , make a big difference in the success of the model.

Note in Eq. 8 that, for any cosmology, a_c is uniquely determined by M_{vir} , independent of a . This implies via Eq. 12 that, for a fixed halo mass,

$$c_{\text{vir}}(a) \propto a. \quad (13)$$

Our model thus predicts that for haloes of the same mass the concentration is proportional to $(1 + z)^{-1}$. This is different from the NFW prediction in which the concentration is a much weaker function of redshift.

In order to gain a basic understanding of the important elements of this model, we discuss its predictions in the context of three cosmological models of increasing complexity: (1) a self-similar model of Einstein-deSitter cosmology and a power-law power spectrum of fluctuations, (2) standard CDM, in which the universe is still Einstein-deSitter but the power spectrum deviates from a power law, and (3) the relevant cosmology of the current investigation, Λ CDM, with $\Omega_m \neq 1$ and a non-power-law spectrum.

3.2 Example 1: the self-similar case

As an illustrative example, assume a fully self-similar case: Einstein-deSitter cosmology, $\Omega_m = 1$, for which the growth rate is $D(a) \propto a$, and a power-law power spectrum of fluctuations, $P(k) \propto k^n$, for which $\sigma(M) \propto M^{-\alpha}$ with $\alpha = (n + 3)/6$. In this case,

$$M_*(a) \propto a^{1/\alpha}. \quad (14)$$

Together with Eqs. 8 and 9, we have $a_c/a_0 = (\mu F)^\alpha$. Then, using Eq. 12, we obtain

$$c_{\text{vir}}(\mu, a) = K(F\mu)^{-\alpha}. \quad (15)$$

Note that in the self-similar case the two parameters F and K can be replaced by one parameter, $KF^{-\alpha}$. Equivalently, we may vary only K and adopt the natural value $F = 1$, namely, apply the model to the collapse of the whole halo. This is a special feature of our revised model, not valid in the original NFW model.

The slope of the function $c_{\text{vir}}(\mu)$ at a is completely determined by the power index α (i.e., n): $c_{\text{vir}} \propto \mu^{-\alpha}$. This simple mass dependence can be checked against the results of the simulations of NFW97 in their Figure 6, which presents $c_{\text{vir}}(\mu)$ at $z = 0$ for Einstein-deSitter cosmology with four different power-law spectra: $n = -1.5, -1, -0.5$, and 0 ($\alpha = 1/4, 1/3, 5/11$ and $1/2$). In each case, our model predicts the simulated slope quite well, even slightly better than the NFW model. As the power-law $M^{-\alpha}$ becomes

steeper (n larger), the difference in collapse epochs for haloes of a given mass difference becomes larger, which is reflected in a steeper $c_{\text{vir}}(\mu)$ relation.

The collapse factor K may be determined from the simulations at the present epoch by matching the value of c_{vir} at any desired μ . We find for a typical simulated halo ($\mu = 1$) at $a = 1$ that $c_{\text{vir}} \simeq 10$, implying that the additional collapse factor for the whole halo ($F = 1$) must be $K \sim 10$.

Clearly, for the fully self-similar case one would expect any dimensionless properties of M_* haloes to be invariant in time. This is easily verified by setting $\mu = 1$ in Eq. 15: $c_{\text{vir}}(1, a) = K$ (for $F = 1$). In this case, the concentration is also fixed for any other fixed value of μ . Accordingly, the concentrations are different for haloes of the *same mass* that are addressed at different redshifts. For the Einstein-deSitter cosmology, Eq. 2 yields $R_{\text{vir}} \propto a$, and then the general behavior of $c_{\text{vir}} \propto a$ (Eq. 13) implies (via Eq. 3) that the value of r_s is the same (in physical coordinates) at all redshifts. Again, this is different from the NFW97 model prediction.

3.3 Example 2: SCDM

As a second example, consider the standard CDM cosmology (SCDM: $\Omega_m = 1$, $h = 0.5$, $\sigma_8 = 0.7$). Although the time evolution here is still self-similar, the power spectrum is not a power law: $\sigma(M)$ has a characteristic bend near $\mu \sim 1$ today [which corresponds to a mass $M_*(a = 1) \simeq 2.5 \times 10^{13} h^{-1} M_\odot$]. The local slope varies from $\alpha \simeq 0$ for $\mu \ll 1$ to $\alpha = 2/3$ for $\mu \gg 1$.

The model solution for $c_{\text{vir}}(\mu)$ does not have a closed form in this case, but it is easy to obtain a useful approximation. The slope of the $c_{\text{vir}}(\mu)$ relation at a specific μ is determined by the effective slope of the power spectrum on a scale corresponding to the mass $\mu F M_*$ (not μM_*), since this is the mass scale used to characterize the halo collapse time in Eqs. 8 and 9). We now obtain an approximate relation similar to Eq. 15, but with the effective local α replacing the constant α :

$$c_{\text{vir}} \simeq K(\mu F)^{-\alpha(\mu F)}. \quad (16)$$

Unlike the power-law example, the value chosen for the constant F does play a role in the slope of the $c_{\text{vir}}(\mu)$ relation at a given a . In order to determine the best values of F and K , we match the model predictions of $c_{\text{vir}}(\mu)$ to the results of the N -body simulations of the SCDM model at the present epoch. Using $F = 0.01$ and $K = 4.3$ in Eqs. 8 and 12, we are able to reproduce quite well the $z = 0$ SCDM results of NFW97 (their Figure 6) over the range $\mu \simeq 0.01 - 100$. The relation about $\mu \sim 1$ is well approximated using Eq. 16, where $\alpha(\mu F = 0.01) \simeq 0.15$.

But now, using no extra parameters, we are also able to reproduce the time dependence of this relation, which we test using the c_{vir} values as determined from our small box ($7.5 h^{-1} \text{Mpc}$) SCDM simulation. In our simulation, we find that the best-fit parameters at $a = 1$ are $F = 0.01$ and $K = 3.8$ (rather than the $K = 4.3$ we found for the NFW97 simulations).[§] For a fixed M_{vir} , we find that the

model-predicted scaling of $c_{\text{vir}}(a) \propto a$ indeed describes very well the time evolution of the halo population.

In our toy model, the values of F and K are assumed to be constants as a function of both a and μ . Such a behavior is naturally expected in the fully self-similar case, in which no special time or scale is present in the problem. However, the success of this toy model in the SCDM case, which is not scale invariant, is somewhat surprising. The reason for this success is linked to the small value of F , which pushes the relevant mass scales of the problem to values much below that of the bend in the power spectrum (near $\mu \sim 1$), where the spectrum is approaching a power-law behavior. For small values of μ ($\mu \lesssim 0.1$), the slope of $c_{\text{vir}}(\mu)$ is almost independent of the actual value of F as long as the latter is smaller than 0.05. The specific preferred value of $F = 0.01$ arises from the need to match the model $c_{\text{vir}}(\mu)$ with the simulations in the range $\mu \geq 1$.

3.4 Example 3: Λ CDM

Our third example concerns a currently popular Λ CDM cosmological model ($\Omega_m = 0.3$, $\Omega_\Lambda = 0.7$, $h = 0.7$, $\sigma_8 = 1.0$, where $M_* \simeq 2 \times 10^{13} h^{-1} M_\odot$ at $z = 0$). In this case, self similarity is violated due to the non-power-law spectrum as before, and also by the time-dependent fluctuation growth rate associated with the low Ω_m . Using similar reasoning to our discussion in the previous example, one may expect our toy model with constant F and K to break down, but, again, this worry is alleviated as long as F is small. As in the SCDM case, this pushes the relevant mass scales to the power-law regime away from the bend in the power spectrum. In addition, a small value of F demands that the collapse epoch is early, when the mean density was near the critical value, $\Omega_m(a_c) \simeq 1$, and therefore the fluctuation growth rate was close to that in the self-similar cosmology, $D(a) \propto a$. The deviation from the self-similar growth rate introduces in Eq. 16 a multiplicative correction factor, given by the growth of fluctuations between the epochs a_c and a in the given cosmology compared to the Einstein-deSitter case. In the case of Λ CDM and $a_c \ll 1$ this factor at $a = 1$ is about 1.25.

As we show in § 5 and § 7 below, using $F = 0.01$ and $K = 4.0$ in the model equations 8 and 12, we are able to reproduce the full behavior of the median $c_{\text{vir}}(\mu, a)$ in our Λ CDM simulations. At $a = 1$, we have $c_{\text{vir}}(\mu) \propto \mu^{-\alpha(F\mu)}$, where $\alpha \simeq 0.13$ for $\mu \sim 1$. For haloes of fixed mass ($\mu M_* = \text{const}$), we have $c_{\text{vir}}(a) \propto a$ as before.

We will show below that by setting the value of K to 2.6 and 6.0 we are able to artificially parameterize the $-\sigma$ and $+\sigma$ scatter respectively in the value of c_{vir} for the simulated population of haloes. A similar range of K values accounts for the scatter for all masses and at all cosmological epochs.

4 SIMULATING HALOES

sults from our large-box ($60 h^{-1} \text{Mpc}$) and small-box ($7.5 h^{-1} \text{Mpc}$) Λ CDM simulations. The presence of large waves induces larger environments of high background density in which the halo concentrations tend to be higher (see § 5).

[§] The normalization of $c_{\text{vir}}(\mu, 1)$ in our simulation is slightly lower than in the NFW simulations, by 15%. This may be due to the small box size; we find a similar effect when we compare re-

4.1 The numerical simulations

Only recently have large cosmological N-body simulations reached the stage where detailed structural properties of many dark-matter haloes can be resolved simultaneously. One of the most successful methods for high force resolution and mass resolution is the Adaptive Refinement Tree (ART) code (KKK97). The method makes use of successive refinements of the grid and time step in high density environments. The simulations based on the ART code provide, for the first time, a compilation of a statistical sample of well-resolved DM haloes, as well as substructure of haloes within haloes. In previous simulations, haloes were picked “by hand” using certain selection criteria from a low-resolution cosmological simulations, to be re-simulated with high resolution. This selection induces a certain bias into the sample.

We have used the ART code to simulate the evolution of DM in a low-density flat Λ CDM model for which $\Omega_m = 0.3$, $\Omega_\Lambda = 0.7$, $h = 0.7$, and $\sigma_8 = 1.0$ at $z = 0$. The simulation followed the trajectories of 256^3 cold dark matter particles within a cubic, periodic box of comoving size $60 h^{-1}\text{Mpc}$ from redshift $z = 40$ to the present. We have used a 512^3 uniform grid, and up to six refinement levels in the regions of highest density, implying a dynamic range of 32,768. The formal resolution of the simulation is thus $f_{\text{res}} = 1.8 h^{-1}\text{kpc}$, and the mass per particle is $m_p = 1.1 \times 10^9 h^{-1}M_\odot$. In the present paper, we analyze 12 saved time steps from $z = 5$ to 0. We have also used two simulations in smaller boxes to check for resolution and cosmology dependence. One of these is a $30 h^{-1}\text{Mpc}$ box simulation of the same Λ CDM cosmology, with 256^3 particles, $m_p = 1.4 \times 10^8 h^{-1}M_\odot$, and $f_{\text{res}} = 0.9 h^{-1}\text{kpc}$. The other, in a $7.5 h^{-1}\text{Mpc}$ box, is of the SCDM cosmology ($\Omega_m = 1$, $h = 0.5$, and $\sigma_8 = 0.7$ at $z = 0$), and it consists of 128^3 particles, $f_{\text{res}} = 0.5 h^{-1}\text{kpc}$, and $m_p = 5.5 \times 10^7 h^{-1}M_\odot$. Tests of the ART code for numerical effects on halo density profiles are discussed in KKBP.

4.2 Finding and fitting haloes and subhaloes

In this investigation, we sample all types of DM haloes independent of their environment. In particular, we identify both the standard kind of “distinct” haloes, of the type identified using common friends-of-friends algorithms and considered in Press-Schechter approximations, and also “subhaloes”, whose centres are located within the virial radius of a larger “host” halo. Our halo finding/classifying algorithm, which is based on the Bound Density Maxima technique (Klypin & Holtzman 1997), has been specifically designed to simultaneously identify distinct haloes and subhaloes (Appendix B).

We fit every identified DM halo using the NFW profile (Eq. 1). Before fitting, we check the halo radial density profile to see if it has a significant upturn, $d\rho(r)/dr > 0$, and if so, we declare this point to be the truncation radius R_t . Our measured R_t values are comparable or somewhat smaller than the expected tidal radii. For haloes with no significant upturn in density, we fit the NFW density profile out to R_{vir} , while for haloes with a truncation radius, we fit the profile out to R_t , and extrapolate the NFW function in order to assign virtual values of R_{vir} and M_{vir} .

The profile fitting is performed as follows. After identifying a centre for the halo, we count particles in logarithmically spaced radial bins, and assign corresponding Poisson errors based on the count in each bin. We then fit an NFW profile (by χ^2 minimization) to the counts in bins using the bin errors in the covariance matrix, and obtain best-fit values for the two free parameters R_{vir} and r_s (or equivalently M_{vir} and c_{vir} , etc.) along with the corresponding errors in these parameters. We then remove unbound particles from each halo, as described in Appendix B, and iterate the process of determining R_t and fitting a profile until the halo contains only bound particles.

We present results for haloes with masses in the range $1.5 \times 10^{11} - 10^{14} h^{-1}M_\odot$; the smallest haloes thus contain $\gtrsim 150$ particles.[¶] A profile fit to a halo of only a few hundred particles may carry large errors. We therefore make a rigorous attempt to estimate the errors and take them into account in every step of the process. Poor fits due to small number statistics are marked by large errors that are incorporated in the analysis and the results we present.

The profile fit of haloes in crowded regions clearly involves ambiguities in the mass assignment to the subhaloes and the host. Our fitting procedure provides a well-defined recipe for mass assignment based on the value of M_{vir} even when the fit is actually performed inside an R_t that is smaller than the R_{vir} obtained by extrapolation.^{||} The concentration parameter is defined in the same way for all haloes, $c_{\text{vir}} = R_{\text{vir}}/r_s$. Because in most cases of subhaloes the extrapolation procedure adds much less mass than the mass that actually lies between R_t and R_{vir} , the double counting is not severe; most of the mass associated with the upturn in the profile is assigned to a different subhalo or to the host. On the other hand, a small subhalo does not cause a significant upturn in the profile of its host halo, and its mass is therefore also included in the mass assigned to the host. This partial double counting introduces some uncertainty to any recipe for assigning a luminous galaxy mass to a halo of a given mass.

The outcome of the halo finder/classifier is a statistical halo catalog that includes all the bound virialized systems in the simulation above the minimum mass threshold. We include distinct haloes and subhaloes, but not subhaloes of a second generation, i.e., those whose hosts are themselves subhaloes of a larger host. The output for each halo includes the list of its bound particles, the location of its centre, the NFW profile parameters (e.g., c_{vir} and M_{vir}), the corresponding errors (σ_c and σ_M), and the truncation radius, if relevant.

[¶] When we extend our analysis down to $5 \times 10^{10} h^{-1}M_\odot$ haloes, we obtain results consistent with trends presented below, but we choose not to include these smaller haloes in our current analysis because our halo catalog is not complete for this mass range.

^{||} For 5% of the subhaloes we actually find $R_t < r_s$. In these cases the errors in the extrapolated values of R_{vir} and M_{vir} become especially large, but they are properly taken into account in the analysis.

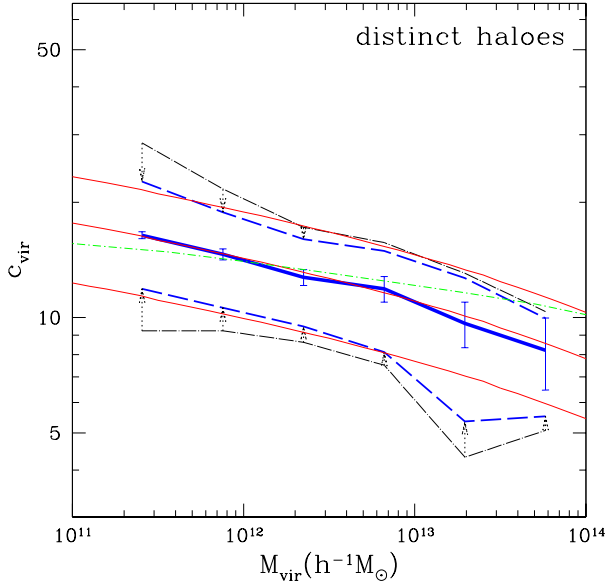


Figure 2. Concentration versus mass for distinct haloes at $z = 0$. The thick solid curve is the median at a given M_{vir} . The error bars represent Poisson errors of the mean due to the sampling of a finite number of haloes per mass bin. The outer dot-dashed curves encompass 68% of the c_{vir} values as measured in the simulations. The inner dashed curves represent only the true, intrinsic scatter in c_{vir} , after eliminating both the Poisson scatter and the scatter due to errors in the individual profile fits due, for example, to the finite number of particles per halo. The central and outer thin solid curves are the predictions for the median and 68% values by the toy model outlined in the text, for $F = 0.01$ and three different values of K . The thin dot-dashed line shows the prediction of the toy model of NFW97 for $f = 0.01$ and $k = 3.4 \times 10^3$.

5 HALO PROFILES TODAY

We start by studying the halo profiles at the current epoch in the simulation. First, we study the median c_{vir} (which is also close to its mean) as a function of mass. Then, the dependence on the environment and on being a subhalo is presented. Finally, we discuss the scatter about the median $c_{\text{vir}}(\mu)$, which leads to a discussion of possible implications on the observed rotation curves and the Tully-Fisher relation in the following section.

5.1 Median relations for distinct haloes

Figure 2 shows $c_{\text{vir}}(M_{\text{vir}})$ at $z = 0$ for distinct haloes. The Poisson errors reflect the number of haloes within each mass bin. In order to account for the fit errors, we generated 500 Monte Carlo realizations in which the measured c_{vir} and M_{vir} of each halo were perturbed using random Gaussian deviates with standard deviations equal to σ_c and σ_M respectively. Median values of c_{vir} were then determined using the Monte Carlo ensemble. The lowest-mass and highest-mass bin have ~ 2000 and 20 haloes respectively (we avoid using bins with less than 10 haloes.), and the Poisson errors grow with mass accordingly.

The median c_{vir} decreases with growing mass, in qualitative agreement with the toy models, and therefore consistent with the assertion that small mass haloes are more concentrated because they typically collapse earlier than haloes of larger masses. The NFW97 model outlined in Appendix A

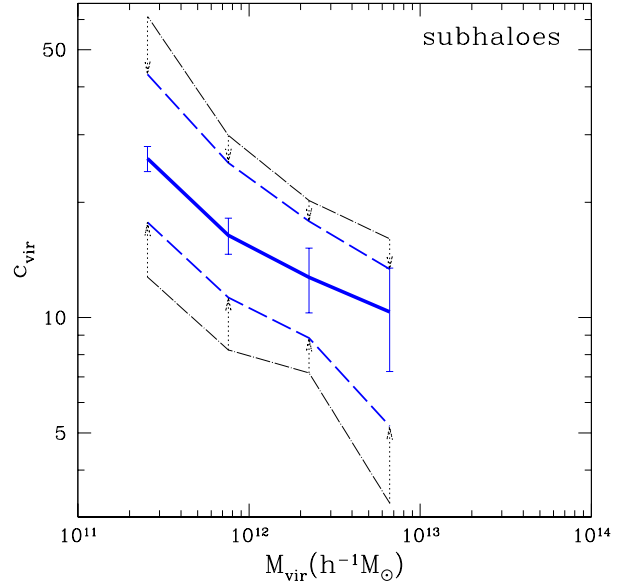


Figure 3. Concentration versus mass for subhaloes at $z = 0$. The curves and errors are the same as in Figure 2.

has been slightly adjusted to yield c_{vir} rather than c_{NFW} . Its predicted slope is in reasonable agreement with that derived from the simulations, but there is some indication that the slope is too shallow. Using our revised toy model outlined in § 3, with $F = 0.01$ and $K = 4.0$, we reproduce the median relation even better, as shown by the central thin solid line. Near $\mu \sim 1$ ($M_{\text{vir}} \sim M_* \simeq 2 \times 10^{13} h^{-1} M_{\odot}$ at $z = 0$), the model prediction is

$$c_{\text{vir}}(\mu, z = 0) \simeq 1.25K (\mu F)^{-\alpha(\mu F)} \simeq 9\mu^{-0.13}. \quad (17)$$

Indeed, the slope of the $c_{\text{vir}}(\mu)$ curve is closely related to the varying slope of the mass power spectrum, which influences the relative difference in collapse epochs for typical objects on different mass scales. The factor of 1.25, as explained in § 3, is a measure of the deviation from the Einstein-deSitter self-similar linear fluctuation growth rate $D(a) \propto a$ between some high redshift and $z = 0$ (where the corresponding collapse epoch, for a given mass, is earlier in the Λ CDM case).

5.2 Subhaloes and environmental dependence

If the median $c_{\text{vir}}(M_{\text{vir}})$ indeed reflects different formation epochs, one might expect the c_{vir} of haloes of a given mass to vary with the density of the environment, since haloes in dense regions typically collapse earlier. In particular, the concentration should tend to be larger for subhaloes compared to distinct haloes. Another effect that may lead to higher c_{vir} values in subhaloes is the expected steepening of their outer profile due to tidal stripping (Klypin et al. 1999; Ghigna et al. 1998; Okamoto & Habe 1998; Avila-Reese et al. 1999). Since stripping is likely to be more effective for small mass haloes, this process may lead to a stronger mass dependence in subhaloes. A third effect is that haloes that are embedded in a high-density environment are likely to experience extreme collapse histories and frequent merger events which may affect their final concentrations.

Figure 3 shows the relation $c_{\text{vir}}(M_{\text{vir}})$ at $z = 0$ for subhaloes. We see that subhaloes on galactic scales ($M_{\text{vir}} \sim$

$10^{12}h^{-1}M_{\odot}$) are indeed more concentrated than distinct haloes of the same mass. The dependence on mass seems to be stronger for subhaloes than for distinct haloes, with $c_{\text{vir}} \propto \mu^{-0.3}$ (compared to $\mu^{-0.13}$), though the large errors in the case of subhaloes make this trend only marginal.

We address directly the dependence of concentration on background density in Figure 4, which shows c_{vir} as a function of local density for all haloes (both distinct and subhaloes) in the mass range $M_{\text{vir}} = 0.5\text{--}1.0 \times 10^{12}h^{-1}M_{\odot}$. The local background density is defined for the dark matter within spheres of radius $1h^{-1}\text{Mpc}$ in units of the average density of the universe in the simulation, $\rho_u = 8.3 \times 10^{10}h^2M_{\odot}/\text{Mpc}^3$. We see that haloes in more dense environments indeed tend to be more concentrated than their more isolated counterparts. Note that this trend is in fact stronger than the dependence of c_{vir} on mass.

We find a similar trend when the local density is determined within spheres of radius $1.5h^{-1}\text{Mpc}$, but the trend becomes weaker when spheres of radius $0.5h^{-1}\text{Mpc}$ are used. Similarly, we find that the trend holds for haloes of mass $\lesssim 5 \times 10^{12}h^{-1}M_{\odot}$. For larger masses, the trend seems to become less pronounced, but this is quite inconclusive because we have only a few massive haloes ($\lesssim 15$) with local densities $\gtrsim 100\rho_u$. A similar trend has been seen for distinct haloes alone, but it is difficult to make a definitive assessment in this case because there are only a few distinct haloes with local densities $\gtrsim 100\rho_u$.

The results at low and high densities are comparable to those for distinct haloes and subhaloes respectively, consistent with a significant correlation between being a subhalo (or a distinct halo) and residing in a low-density (or a high-density) environment.

Our toy model is not sophisticated enough to account for the dependence of concentration on environment, and for the exact relation for subhaloes. However, in the framework of our toy model (§ 3), we can artificially parameterize these trends by varying the collapse parameter K as a function of local density. We are left with the qualitative speculations mentioned above for the interpretation of the trends with environment seen in the simulations.

We discuss possible implications of the environment dependence in § 8.

5.3 Scatter in the concentration parameter

One of the most interesting of our results at $z = 0$ is the spread in c_{vir} values for fixed M_{vir} . A significant scatter about the median relations may have intriguing observational implications. Before we report on our results, we briefly describe our methods of ascertaining the intrinsic scatter.

There are two sources of scatter on top of the intrinsic spread in halo concentrations. First, Poisson noise due to the sampling of a finite number of haloes in each mass bin adds a significant spread, especially in the case of large-mass haloes. Small-mass haloes, on the other hand, are plentiful, but the relatively small number of particles in each halo introduces a significant error in the measured value of the halo profile parameters M_{vir} and c_{vir} . This is the second source of additional scatter. The Poisson error due to the finite number of haloes is relatively straightforward to correct, but correcting

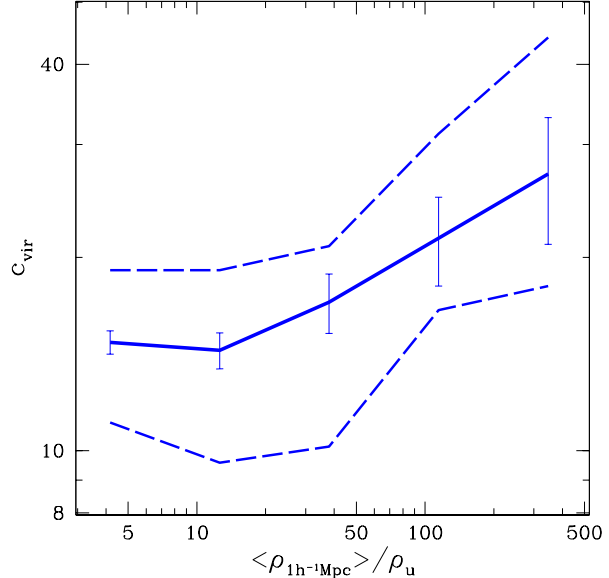


Figure 4. Concentrations versus environment. The concentration at $z = 0$ of all haloes in the mass range $0.5 - 1.0 \times 10^{12}h^{-1}M_{\odot}$ as a function of local density in units of the average density of the universe. The local density was determined within spheres of radius $1h^{-1}\text{Mpc}$. The solid line represents the median c_{vir} value, the error bars are Poisson based on the number of haloes, and the dashed line indicates our best estimate of the intrinsic scatter.

the error in the profile parameters requires a more involved procedure.

We account for this error in the profile parameters using the errors obtained in the profile fits. Within each mass bin, we have performed ~ 500 Monte Carlo realizations in an attempt to undo the effect of the measurement errors as follows. Every measured c_{vir} value has been perturbed by a one-sided random Gaussian deviate, positive or negative depending on whether the measured c_{vir} is smaller or larger than the median respectively. The standard deviation of each Gaussian deviate was set to be the error in the value of c_{vir} as estimated in the profile fit of that specific halo. The smaller scatter obtained in this set of Monte Carlo realizations provides an estimate for the spread excluding the fit errors. We then subtract in quadrature the Poisson error due to the finite number of haloes to obtain our estimate for the intrinsic scatter in c_{vir} .

We have checked our technique of measuring the intrinsic spread using an artificial ensemble of 1000 (spherical) haloes with a variety of numbers of particles and a known intrinsic distribution of c_{vir} . The technique reproduced the median concentration and true spread to within 5% when the particle number was varied from 100 to 10^5 , the range of interest for our simulated haloes.

We have also checked our procedure for measuring the intrinsic scatter using a simulation of higher resolution in a smaller box of side $30h^{-1}\text{Mpc}$, in which there are on average 8 times as many particles in a halo of a given mass. This simulation was stopped at $z = 1.7$, so we pursued this test only at that epoch and earlier. Because the simulation of higher resolution contains only few haloes near the high mass end, we limit the comparison to the mass range $(3\text{--}10) \times 10^{11}M_{\odot}$. The values obtained by our procedure from the haloes simulated with higher resolution, both for the me-

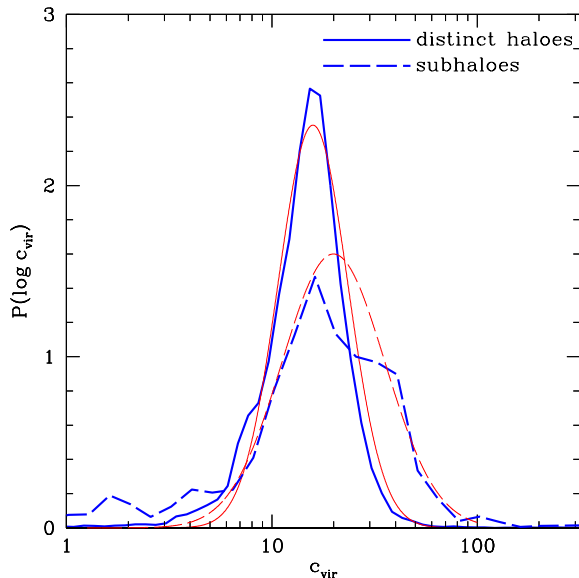


Figure 5. The probability distributions of distinct haloes (solid line) and subhaloes (dashed line) at $z = 0$ within the mass range $(0.5 - 1.0) \times 10^{12} h^{-1} M_{\odot}$. The simulated distributions (thick lines) include, the $\sim 2,000$ distinct haloes and ~ 200 subhaloes within this mass range. Log-normal distributions with the same median and standard deviation as the measured distributions are shown (thin lines). Subhaloes are, on average, more concentrated than distinct haloes and they show a larger spread.

dian and the intrinsic spread in c_{vir} , agree to within $\sim 5\%$ with the corresponding values obtained with lower resolution. This level of agreement is consistent with the Poisson error of the high-resolution simulation, which is of order 10% in the mass range we consider.

Note that what we treat as measurement error in the profile fit actually includes scatter due to real deviations of the halo structure from a purely spherical NFW profile, which we should probably regard as part of the intrinsic scatter. This means that our estimated intrinsic scatter is a conservative underestimate.

Now that the method has been discussed, we turn the attention back to the relation between c_{vir} and M_{vir} for distinct haloes, Figure 2. The measured 68% scatter is shown, as well as the “pushed in” corrected scatter which marks our (under-) estimated intrinsic scatter. As can be seen by noting the Poisson error bars, the correction at the small-mass end is almost entirely due to the measurement errors of the profile parameters, which are dominated by the small number of particles per halo.

We see that the intrinsic spread is large; it is comparable to the systematic change in the median value of c_{vir} across the entire mass range studied. In addition, the spread is roughly constant as a function of mass, with a 1σ deviation of $\Delta(\log c_{\text{vir}}) \sim 0.18$. We discuss possible observational implications of this scatter in the next section.

The spread in c_{vir} values as a function of M_{vir} for subhaloes is shown in Figure 3. Note that the scatter is larger for the subhalo population than for their distinct counterparts of the same mass, with a 1σ variation of $\Delta(\log c_{\text{vir}}) \sim 0.24$. This is clearly seen in Figure 5, where the probability distributions of concentrations for distinct haloes and subhaloes are compared (for $M_{\text{vir}} = 0.5 - 1.0 \times 10^{11} h^{-1} M_{\odot}$). It is

possible that the larger scatter evaluated for subhaloes is a result of their more complicated formation histories, including for example more interactions and stripping. We point out that we have found no significant trend with the number of co-subhaloes within the same virialized host. Such a trend might have been expected if interaction among co-subhaloes plays an important role in determining the profile shape.

The 68% intrinsic spread in c_{vir} as a function of the local density (for $0.5 - 1.0 \times 10^{12} h^{-1} M_{\odot}$ haloes) is given in Figure 4. We can use the obtained distribution of halo concentrations as a function of local density to probe questions associated with the origin of LSB galaxies and the observed morphology density relation (§ 8).

In Figure 5 we show the distribution of concentration values for distinct haloes and subhaloes, along with log-normal functions with the same median and standard deviation. The log-normal forms describe the observed distributions reasonably well. Such a result has also been reported by Jing (1998). Our scatter for distinct haloes is similar to that reported by Jing, but it is difficult to make a quantitative comparison because the two investigations focus on different aspects of the problem.

In the context of the toy model presented in § 3, one can parameterize the spread in c_{vir} as spread in collapse epochs and/or collapse histories, via the parameters a_c and K respectively. Using Eq. 12, we find that the evaluated spread in c_{vir} can be matched by a spread of $\Delta[\log K(a_0/a_c)] \simeq \Delta(\log c_{\text{vir}}) \sim 0.18$ in the toy model. If we absorb all the scatter in the collapse parameter K , we find that the model matches the $50 \pm 34\%$ (encompassing 68%) percentiles of the c_{vir} distribution with $K = 6.0$ and 2.6 respectively (for $F = 0.01$). Note that the scatter in K is not symmetric about the median (of $K = 4.0$); it rather reflects the log-normal nature of the c_{vir} distribution. The model predictions for the above values of K are shown as thin solid lines in Figure 2; they match the simulated scatter fairly well. We show in § 7 that this parameterization also reproduces the simulated scatter as a function of z . This is just a useful parameterization of the scatter using the toy model. A more detailed modelling of the spread with deeper physical insight is beyond the scope of the present paper.

6 ROTATION CURVES AND TULLY-FISHER

The simulated distributions of c_{vir} values as a function of mass and environment have several observational implications. Here, we discuss only preliminary predictions involving rotation curves and the Tully-Fisher relation based on very crude assumptions about associating disc properties to those of the simulated dark-matter haloes. A more detailed study requires realistic modelling of physical processes involving gas and stars.

In order to illustrate what the spread in c_{vir} values may imply observationally, Figure 6 shows example NFW rotation curves for $3 \times 10^{11} h^{-1} M_{\odot}$ (distinct) haloes using the median, $\pm 1\sigma$, and $\pm 2\sigma$ values of c_{vir} . These are raw rotation curves of the dark-matter haloes before they are affected by the infall of baryons, but they may still serve as a crude approximation for the final rotation curves. One can see that the rotation curves span a significant range of shapes and the corresponding spread in V_{max} values is substantial. The

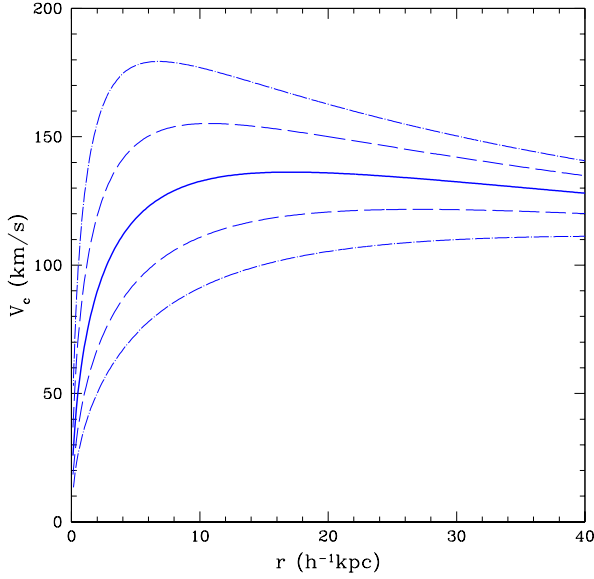


Figure 6. The spread in NFW rotation curves corresponding to the spread in concentration parameters for distinct haloes of $3 \times 10^{11} h^{-1} M_{\odot}$ at $z = 0$. Shown are the median (solid), $\pm 1\sigma$ (long dashed), and $\pm 2\sigma$ (dot-dashed) curves. The corresponding median rotation curve for subhaloes is comparable to the upper 1σ curve of distinct haloes.

median rotation curve for $3 \times 10^{11} h^{-1} M_{\odot}$ subhaloes (not shown) is similar to the upper 1σ curve shown in Figure 6.

A clue for the expected TF relation of discs may be provided by the measured relation between the halo parameters M_{vir} and V_{max} . The latter is derived from c_{vir} using Eq. 6. The $M_{\text{vir}}-V_{\text{max}}$ relation is shown in Figure 7, separately for distinct haloes and subhaloes. The median distinct-halo relation is well approximated by the linear relation

$$\log[M_{\text{vir}}/(h^{-1} M_{\odot})] = \alpha \log[V_{\text{max}}/(\text{km/s})] + \beta \quad (18)$$

with $\alpha \simeq 3.4 \pm 0.05$ and $\beta \simeq 4.3 \pm 0.2$, where the Poisson errors in each mass bin have been propagated to obtain the quoted error on each fit value. Note that the slope is steeper than that expected from the standard scaling of the virial parameters: $M_{\text{vir}} \propto V_{\text{vir}}^3$. This is a direct result of the correlation between mass and concentration ($M_{\text{vir}} \propto c_{\text{vir}}^{-0.13}$). We may in fact derive the expected α using the effective power law from Eq. 6: $V_{\text{max}}/V_{\text{vir}} \propto c_{\text{vir}}^{0.27}$; which implies $M_{\text{vir}} \propto V_{\text{max}}^3 (V_{\text{vir}}/V_{\text{max}})^3 \propto V_{\text{max}}^3 c_{\text{vir}}^{-0.81} \propto V_{\text{max}}^{3.4}$. We point out that the linear relation provides a good fit, showing no obvious need for non-linear corrections in the TF relation.

The lower panel in Figure 7 shows M_{vir} vs. V_{max} for subhaloes. This relation is also well fit by the linear relation, Eq. 18, but now with $\alpha \simeq 3.9 \pm 0.25$ and $\beta \simeq 2.6 \pm 0.75$. The subhalo relation has a steeper slope compared to distinct haloes, and $M_{\text{vir}} \simeq 10^{12} h^{-1} M_{\odot}$ subhaloes typically have a $\sim 12\%$ higher V_{max} . This difference between the slope and zero-point of distinct haloes and subhaloes may have implications for the use of cluster or group galaxies to calibrate the Tully-Fisher relation in the field.

We point out, however, that if for subhaloes we replace M_{vir} by the mass M_t inside the truncation radius R_t , the logarithmic slope becomes $\alpha_t = 3.6 \pm 0.2$, consistent with the slope obtained by Avila-Reese et al. (1999) for haloes within clusters using a similar mass assignment procedure.

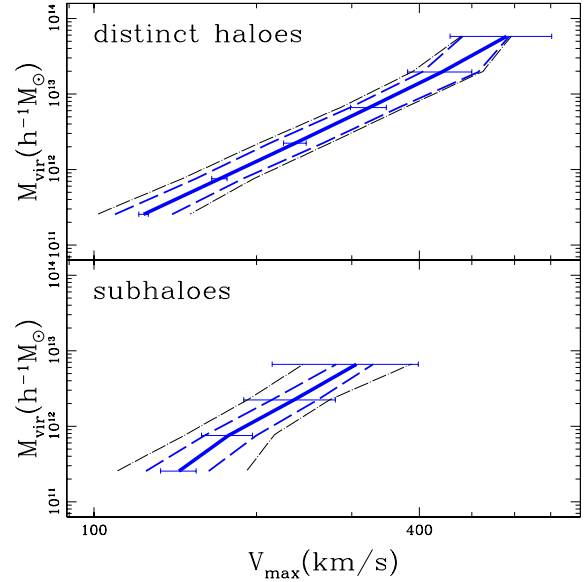


Figure 7. Virial mass versus V_{max} at $z = 0$ for distinct haloes (a) and subhaloes (b). The outer dot-dashed and dark dashed lines indicate the measured and corrected intrinsic 68% scatter respectively.

(The reason for the slope change is that the ratio of M_t/M_{vir} is roughly 1 for low-mass, high- c_{vir} haloes, and becomes less than 1 for high-mass, low- c_{vir} haloes.) This slope is similar to the slope we find for distinct haloes. It is not obvious a priori which of the halo masses is more relevant to the mass of the cooled gas that ends up as the luminous disc, and thus to the observed Tully-Fisher relation. Therefore, the worry about the universality of the slope of Tully-Fisher is not conclusive. However, the zero-point difference between the two types of haloes exists regardless of the mass choice, and is a robust result.

The scatter in the TF relation is an issue of great interest. We find for distinct haloes a 1σ scatter at fixed V_{max} of $\Delta(\log M_{\text{vir}}) \simeq 0.17$, while the corresponding scatter for fixed M_{vir} is $\Delta V_{\text{max}}/V_{\text{max}} \simeq 0.12$. This scatter is in rough agreement with the spread predicted by Eisenstein & Loeb (1996) for a similar cosmology using Monte Carlo realizations of halo formation histories based on the Press-Schechter approximation. The subhalo relation shows an even larger scatter, with $\Delta V_{\text{max}}/V_{\text{max}} \simeq 0.16$ at a fixed M_{vir} .

Observational estimates for the intrinsic scatter in (I-band) TF range from $\sigma(V)/V \sim 0.09$ (Willick et al. 1996) to ~ 0.03 (Bernstein 1994). At best, the observed scatter leaves no room for any intrinsic variation in the mass-to-light ratio of galaxies, and may imply that gas contraction and other hydrodynamical processes must somehow act to decrease the scatter. A simple idea that may resolve this discrepancy is discussed in Appendix C and we briefly outline the argument here. For a fixed mass and spin, a more concentrated halo (higher V_{max}) will induce more gas contraction, and therefore produce a smaller, brighter disc. Such a correlation between the mass-to-light ratio of galaxies and the deviation of V_{max} from the median V_{max} at a given M_{vir} could reduce the scatter to that required to match observations. Detailed modelling, including the back-reaction of the halo during disc formation, is needed to test this hypothesis in detail.

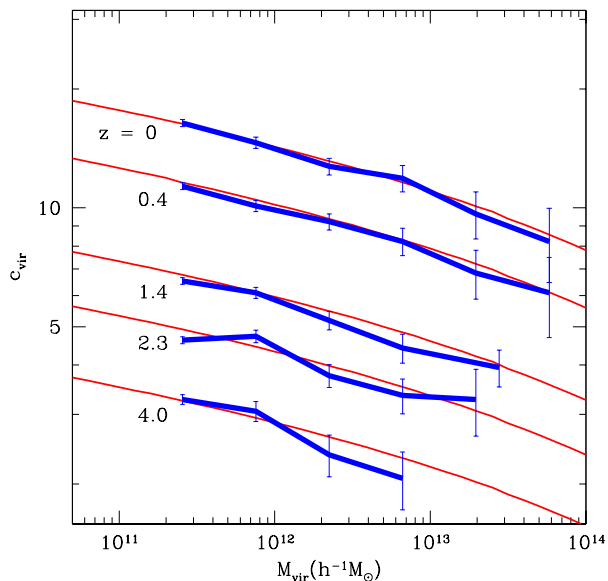


Figure 8. Median c_{vir} values as a function of M_{vir} for distinct haloes at various redshifts. The error bars are the Poisson errors due to the finite number of haloes in each mass bin. The thin solid lines show our toy model predictions.

7 REDSHIFT DEPENDENCE

As data accumulate at high redshift, it becomes increasingly important to study the predicted evolution of the population of halo profiles as a function of redshift.

Figure 8 shows the median c_{vir} as a function of M_{vir} for distinct haloes at several different redshifts. We see that for a fixed mass, the typical c_{vir} value changes quite dramatically, while the shape of the mass dependence remains roughly constant. The thin solid lines show our toy model predictions. This two-parameter model, which has been normalized to match the slope and normalization of the relation at $z = 0$, does remarkably well at all redshifts. As predicted by the toy model in § 3, the concentration of haloes of a fixed mass scales as $c_{\text{vir}} \propto (1+z)^{-1}$. A similar behavior has been confirmed using the SCDM simulation in a smaller box ($7.5h^{-1}\text{Mpc}$, described in § 4). The redshift dependence of the subhalo concentrations seems similar, but we don’t have sufficient statistics for conclusive results involving subhaloes at high redshifts.

As mentioned in the Introduction, the dramatic evolution in the concentration of haloes of a fixed mass is different from the prediction of the NFW97 analytic toy model (see Appendix A). This is illustrated in Figure 9, which shows the median c_{vir} of the distinct halo population of $M_{\text{vir}} = (0.5 - 1.0) \times 10^{12} h^{-1} M_{\odot}$ as a function of redshift. The NFW prediction (for $0.8 \times 10^{12} h^{-1} M_{\odot}$ haloes) overestimates c_{vir} by $\sim 50\%$ at $z = 1$, and the disagreement grows with redshift. Our revised toy model reproduces the simulated redshift trend very well. The scatter about the relation is remarkably constant as a function of z : $\Delta(\log c_{\text{vir}}) \sim 0.18$. Also shown is how the spread can be parameterized by varying K in our toy model, as discussed in § 5.

The redshift dependence of the inner radius, r_s , can be deduced from that of c_{vir} by recalling that the virial radius of fixed-mass haloes also varies like $R_{\text{vir}} \propto \Delta_{\text{vir}}^{1/3}/(1+z)$. This implies that, on average, the inner radius of haloes of a

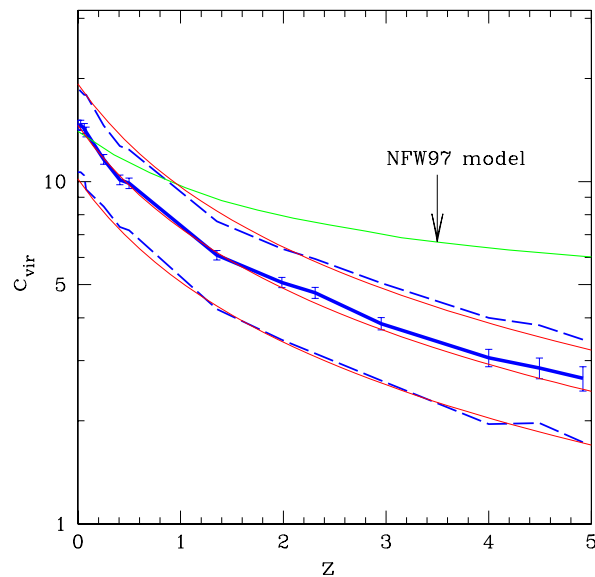


Figure 9. Concentration as a function of redshift for distinct haloes of a fixed mass, $M_{\text{vir}} = 0.5 - 1.0 \times 10^{12} h^{-1} M_{\odot}$. The median (heavy solid line) and intrinsic 68% spread (dashed line) are shown. The behavior predicted by the NFW97 toy model is marked. Our revised toy model for the median and spread for $8 \times 10^{11} h^{-1} M_{\odot}$ haloes (thin solid lines) reproduces the observed behavior rather well.

given mass remains roughly constant as a function of redshift (aside from the z dependence of Δ_{vir}). We see this explicitly in Figure 10, which shows the evolution of the median and 68% scatter of r_s as a function of z for distinct haloes in the mass range $0.5 - 1.0 \times 10^{12} h^{-1} M_{\odot}$. The fact that the median r_s value declines slightly near $z = 0$ is due to the z dependence of Δ_{vir} in the ΛCDM model simulated. The robustness of the characteristic length scale, r_s , may provide an interesting clue for the understanding of the build-up of DM halo structure.

The strong decline in the concentration of haloes of a fixed mass as a function of redshift should have an interesting impact on galaxy-formation modelling at high redshift — e.g., aimed at understanding the nature of Lyman Break Galaxies (Steidel et al. 1996; Lowenthal et al. 1997) and the evolution of the Tully-Fisher relation (Vogt et al. 1997). Although, in general, haloes, and therefore galaxies, are expected to be smaller at high redshift (reflecting the higher universal density) and to have higher circular velocities ($V_{\text{vir}} \propto R_{\text{vir}}^{-1/2}$), the observed c_{vir} behavior will tend to counteract this tendency.

Insight into the expected TF evolution of discs may be gained from Figure 11, which shows the M_{vir} versus V_{max} relation for (distinct) haloes at several redshift steps. The evolution in the zero-point is indeed less dramatic than would be expected from the scaling of V_{vir} . In fact (not shown) there is almost no evolution in the zero-point between $z = 0 - 0.5$. The slope of the relation is roughly constant as a function of redshift ($\alpha = 3.4 \pm 0.1$) and the scatter is roughly constant; $\Delta V_{\text{max}}/V_{\text{max}} \simeq 0.12$.

Furthermore, because disc size is expected to be a decreasing function of halo concentration (§8), the decline of c_{vir} with z implies a relative increase in disc sizes at high redshift. This should result in lower than expected surface

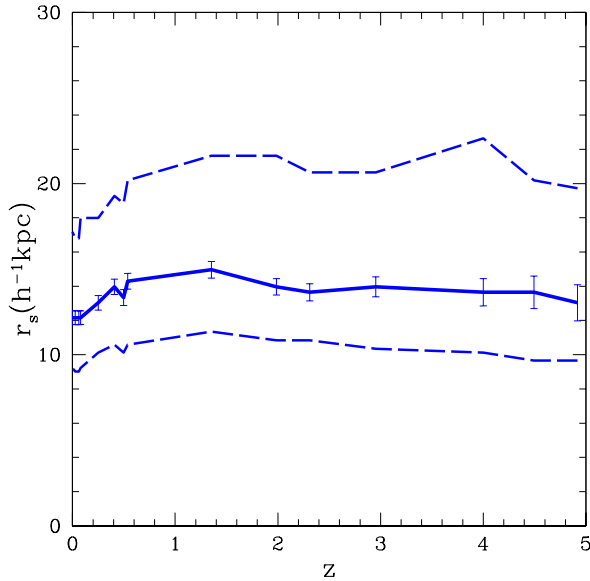


Figure 10. The inner radius r_s as a function of redshift for distinct haloes of fixed mass, $M_{\text{vir}} = 0.5 - 1.0 \times 10^{12} h^{-1} M_{\odot}$. Shown are the median (solid line) and intrinsic 68% spread (dashed lines). The median value for r_s remains approximately constant as a function of redshift.

brightnesses at high z , both because of the extended size and the corresponding lower efficiency of star formation. To this one could add the fact that the supply of cold gas for disc formation at high redshifts may be limited (not extending all the way to R_{vir}) because the smaller inner densities will lessen collisional cooling. These results may hinder the association of quiescently star-forming objects with Lyman-break galaxies as discussed e.g., by Mo, Mao, & White (1999) (see Kolatt et al. 1999b; Somerville, Primack, & Faber 1999 for an alternative physical model for Lyman-break galaxies). They further argue for the slow evolution of the Tully-Fisher relation.

8 CONCLUSIONS AND DISCUSSION

The main direct conclusions of this paper, based on analyzing a statistical sample of dark-matter haloes in a high-resolution simulation of the Λ CDM cosmology, are as follows:

- The redshift dependence of the halo profile parameters has been measured in the simulations, and reproduced by an improved toy model. For example, $c_{\text{vir}} \propto (1+z)^{-1}$ for haloes of the same mass, predicting that at high redshift they are less concentrated and with larger inner radii than previously expected. The corresponding prediction for rotation curves is lower values of $V_{\text{max}}/V_{\text{vir}}$ at high z .
- The correlation between any two halo profile parameters has a significant scatter. For example, in the $c_{\text{vir}}-M_{\text{vir}}$ relation, the spread in c_{vir} is comparable to the systematic change in c_{vir} across three orders of magnitude in M_{vir} . The 1σ spread for fixed M_{vir} is $\Delta(\log c_{\text{vir}}) \simeq 0.18$, corresponding to $\Delta V_{\text{max}}/V_{\text{max}} \simeq 0.12$ at a given M_{vir} .
- There are indications for environmental trends in halo profiles. Haloes in dense environments, or subhaloes, are

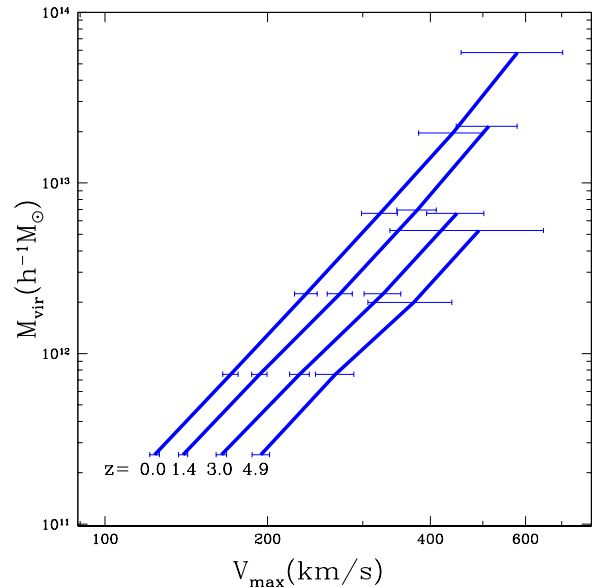


Figure 11. The evolution of the distinct halo Tully-Fisher relation, M_{vir} versus V_{max} , for several redshift steps. The evolution is weaker than the M_{vir} versus V_{vir} relation because c_{vir} falls rapidly with redshift (Fig. 9).

more concentrated than their isolated counterparts of the same virial mass, and they exhibit a larger scatter in c_{vir} .

The main implications of the above findings can be summarized as follows:

- Disc galaxies at high redshifts are predicted to be more extended and of lower surface brightness than expected previously. The constant inner radius at fixed mass may be a dynamical clue for understanding the formation of halo structure.
- The scatter in the halo mass-velocity relation is significantly larger than in the observed TF relation, which suggests that the luminosity of a disc forming inside a halo of a given mass should correlate with the maximum rotation velocity. We pointed out a possible simple explanation for that.
- The environmental trends of halo profiles may caution against the universality of the TF relation. In addition, these trends, together with the observed scatter, may provide insight into the origin of the Hubble sequence. Below, we argue that haloes of low concentration will tend to host blue galaxies and haloes of high concentration, red galaxies or spheroids. We also point out that extremely low c_{vir} haloes plausibly host LSB galaxies.

We have proposed an alternative to the toy model originally proposed by NFW97. It reproduces the correlations between the two parameters of the halo profiles, e.g. c_{vir} and M_{vir} , as well as the redshift dependence of these correlations. This model also offers a simple parameterization that reproduces the scatter about the median relation observed in our simulation. The modified toy model is a useful tool for semi-analytic modelling of galaxy formation. In particular, analyses of the type performed by Mo et al. 1999, which made predictions for disc properties at $z \sim 3$, based on the halo toy model of NFW97, should be reconsidered using our modified toy model.

The large intrinsic scatter we find in the correlations between the halo profile parameters makes the haloes a two-parameter family, as expected, and should be taken into account when trying to model the scatter in observable properties of galaxies (c.f. Mo, Mao, & White 1998; Navarro 1998; Navarro & Steinmetz 1999).

In order to gain a qualitative understanding of how c_{vir} may affect galactic disc formation, we may assume that the exponential disc forms by the adiabatic contraction of gas inside the dark-matter halo (Blumenthal et al. 1986; Flores et al. 1993; Dalcanton, Spergel, & Summers 1997; Mo et al. 1998). The final disc size, r_{d} , can be derived from the halo parameters c_{vir} and R_{vir} , under the following further assumptions that (a) the disc forms from cold gas of mass $\sim 0.03M_{\text{vir}}$ which follows the original density profile of the halo out to R_{vir} , and (b) the specific angular momentum of the gas is equal to that of the halo, which has an original spin parameter of $\lambda = 0.035$. Under these assumptions, we find the following fitting formula is good to within 1% for $1 < c_{\text{vir}} < 50$ (Bullock et al. 1999b):

$$r_{\text{d}} \simeq 5.7 h^{-1} \text{kpc} \left(\frac{R_{\text{vir}}}{100 h^{-1} \text{kpc}} \right) [1 + (c_{\text{vir}}/3.73)^{0.71}]^{-1}. \quad (19)$$

(A similar fitting formula, which allows more varied assumptions about the halo and disc make-up, is provided by Mo et al. 1998.) The general result is that r_{d} , and thus the disc surface brightness, is a decreasing function of c_{vir} .

The spread in exponential disc sizes implied from our 68% spread in concentration values for an $R_{\text{vir}} = 200 h^{-1} \text{kpc}$ halo at $z = 0$ ($M_{\text{vir}} \sim 10^{12} h^{-1} M_{\odot}$, $c_{\text{vir}}:9.2 \rightarrow 21.3$) is $r_{\text{d}} : 4.0 \rightarrow 2.6 h^{-1} \text{kpc}$. This is roughly the same spread in disc sizes resulting from a spin parameter variation of $\lambda : 0.05 \rightarrow 0.03$, which is approximately the intrinsic spread in λ inferred from N-body simulations (Barnes & Efstathiou 1987; Warren et al. 1992; Bullock et al. 1999a).

The two quantities, c_{vir} and λ , are thus of comparable importance for determining observable properties of galaxies, and define a plane in parameter space for haloes of fixed mass. We suggest that the $c_{\text{vir}}-\lambda$ plane can perhaps be linked to the observed variations of galaxies and help explain the Hubble sequence. For example, we argued above that haloes with very low concentrations would tend to lead to discs of low surface brightness, and with slowly rising rotation curves (i.e., $V_{\text{max}}/V_{\text{vir}} \sim 1$). This argument will only apply, however, if λ is sufficiently large to prevent extensive gas infall. Similarly, haloes of high- c_{vir} and low- λ will likely be unable to produce dynamically stable discs (see, e.g., Mo et al. 1998), and instead host spheroids. Other combinations of these parameters, may, perhaps, lead naturally to a range of galaxy morphologies.

This kind of mapping is further motivated by the understanding that high- c_{vir} haloes collapse earlier than low- c_{vir} haloes (as predicted by the toy model and explicitly demonstrated by NFW97 using simulated haloes). A natural association is then that high- c_{vir} haloes host old, red galaxies, and lower- c_{vir} haloes host young, blue galaxies. Furthermore, the environmental trend, that haloes in low-density environments tend to be less concentrated than haloes of the same mass in high-density environments, fits nicely into this picture. Indeed, LSB galaxies are observed to be more isolated than galaxies of higher surface brightness (Bothun et al. 1993; Mo et al. 1994), and spheroids tend to inhabit

high-density environments (Dressler 1980; Postman & Geller 1984).

We have made in this paper only crude preliminary attempts to study the implications of our results concerning halo profiles. It would be desirable to incorporate our measured halo properties into semi-analytic modelling of gas processes and star formation in order to make detailed predictions for observable galaxy properties and their evolution.

ACKNOWLEDGMENTS

We would like to thank Marc Davis, Daniel Eisenstein, Sandy Faber, Avi Loeb, Ari Maller, Jason Prochaska, David Spergel, Risa Wechsler, and David Weinberg for helpful discussions and comments. The simulations were performed at NRL and NCSA. This work was supported by grants from NASA and NSF at UCSC and NMSU, and by Israel Science Foundation and US-Israel Binational Science Foundation grants.

APPENDIX A: THE NFW97 MODEL

For completeness, we briefly review the NFW prescription for determining $c_{\text{vir}}(M, a)$. The goal of the NFW procedure is to provide the density profile of a halo of mass M_{vir} at epoch a_0 assuming that the profile is of the NFW form (1). The collapse redshift is now determined using the Press-Schechter approximation, which, given M_{vir} at epoch a_0 , can be used to approximate the probability distribution for the epoch a when a halo trajectory was first more massive than some fraction f of M_{vir} (Lacey & Cole 93)

$$P(> f M_{\text{vir}}, a | M_{\text{vir}}, a_0) = \text{erfc} \left[\frac{\delta_{\text{crit}}(a) - \delta_{\text{crit}}(1)}{\sqrt{2(\sigma_0^2(f M_{\text{vir}}) - \sigma_0^2(M_{\text{vir}}))}} \right]. \quad (\text{A1})$$

The quantities σ_0 and δ_{crit} are defined in § 3. One determines a_c , by solving Eq. A1 for the *most probable* value of a by setting $P(> f M, a_c | M, a_0) = 0.5$. One now assumes that the central density of the halo is proportional to the density of the universe at a_c , which implies:

$$\rho_s = k \rho_u(a_0) \left[\frac{a_c}{a_0} \right]^3, \quad (\text{A2})$$

where k is a numerical constant. Now, given M_{vir} and a_0 , Eqs. A1 and A2 determine ρ_s and thus completely specify the density profile.

This procedure has two free parameters, f and k , which may be adjusted in order to match the slope and normalization respectively of $c_{\text{vir}}(M)$ at $a = 1$. NFW97 show that this two parameter model reproduces the $a = 1$ relations of simulated haloes in various cosmologies, including power law and open models. For the Λ CDM model we discuss, their favorite parameters are $f = 0.01$ and $k = 3.4 \times 10^3$, and these provide a reasonable reproduction of the median $c_{\text{vir}}(M)$ relationship at $a = 1$ in our simulations.

Although useful in its ability to provide the correct $z = 0$ relation, this model fails to reproduce the observed z evolution of halo concentrations (§ 7). In § 3, we present a revised toy model which, using the same number of free parameters, reproduces the full observed behavior of $c_{\text{vir}}(M, z)$.

APPENDIX B: THE HALO FINDER

Most commonly used halo finders, which work either by the location of overdensities in a spatial window of fixed shape (usually spherical) or by friends-of-friends algorithms, do not account for haloes within haloes. Since our projects specifically address the question of substructure, we have been obliged to devise a halo finder and classification algorithm suited for this purpose.

If one were only interested in distinct, virialized objects, haloes would be easily identified — there is little confusion as to where one halo ends and another begins because the physical extent of an object is determined by the virial overdensity criterion. However, we are interested in objects within the virial radius of large haloes, therefore certain ambiguities arise. How close must two density maxima be in order for them to represent a single object? How does one differentiate substructure from a collision in progress? How does one assign mass to haloes and subhaloes appropriately?

We have found a solution to these problems by assigning to each halo two length scales — an inner radius, r_s , and an outer radius R_{vir} . We do so by modelling the density profile of each halo using Eq. 1. The virial radius R_{vir} determines each halo mass and radial extent, and r_s determines when two density maxima/haloes should be combined into one. The details are described below.

Because the modelling process requires fitting a density profile to each halo, we attempt to find only haloes with more than N_p^{min} particles within their virial radii. If m_p is the mass of each particle, this means the minimal virial mass of haloes identified is $M_{\text{halo}}^{\text{min}} = N_p^{\text{min}} \times m_p$. Equivalently, using Eq. 2, we have a minimum virial radius $R_{\text{vir}}^{\text{min}}$. The value of N_p^{min} is the first free parameter of this algorithm. We use $N_p^{\text{min}} = 50$.

Our density maxima finding routine is based on a the BDM (Klypin & Holtzman 1997) algorithm. We outline our procedure below, including our precise methodology which is generalizable for any simulation parameters and our detailed procedure for defining and classifying haloes.

(i) We construct density field values by a Cloud-in-Cell (CIC) process (Hockney & Eastwood 1981) on the largest grid of the simulation ΔL , and rank the particles according to their local density as determined on this grid.

We then search for the possible halo centres, using two sets of smoothing spheres; one, with a small radius, r_{sp1} , in order to locate of tight, small clumps; and the other, with a larger radius, r_{sp2} , in order to locate the centres of haloes with diffuse cores. The smaller radius is $r_{\text{sp1}} = \alpha f_{\text{res}}$, where f_{res} is the highest force resolution in the simulation and α is a free parameter of order unity. We use $\alpha = 2$. The second set of spheres have $r_{\text{sp2}} = R_{\text{vir}}^{\text{min}}$.

For each set of spheres, we take from the ranked list the particle with the highest local density and place a sphere about its location. A second sphere is placed about the next particle in the list not contained in the first sphere. The process is continued until all of particles are contained within at least one sphere. Because we are only interested in centres of haloes more massive than $M_{\text{vir}}^{\text{min}}$, we discard each sphere with fewer than a set number of particles. The minimum number of particles required for a kept sphere is determined separately for each radius.

For the r_{sp1} spheres, we use the following conservative

halo density profile:

$$\rho(r) = \begin{cases} C/r_{\text{sp1}}^{2.5} & r < r_{\text{sp1}} \\ C/r^{2.5} & r > r_{\text{sp1}}, \end{cases} \quad (\text{B1})$$

(where C is determined by fixing the minimum halo mass to be $M_{\text{vir}}^{\text{min}}$), in order to estimate the minimum core number of particles within r_{sp1} :

$$N_{\text{sp1}} = \frac{N_p^{\text{min}}}{1 + 6[(R_{\text{vir}}^{\text{min}}/r_{\text{sp1}})^{1/2} - 1]}. \quad (\text{B2})$$

For the $z = 0$ timestep of the $60h^{-1}$ Mpc simulation we analyze, $N_{\text{sp1}} = 3.9 \rightarrow 3$. Spheres of size r_{sp1} with fewer than N_{sp1} particles are discarded. Similarly, all of the r_{sp2} spheres containing fewer than $N_{\text{sp2}} = N_p^{\text{min}}$ particles are discarded.

The final list of candidate halo centres is made up of all of the (small) r_{sp1} spheres, together with each of the r_{sp2} spheres that *does not* contain an r_{sp1} sphere.

(ii) For each sphere of radius $r_{\text{sp}} = r_{\text{sp1}}$ or r_{sp2} , whichever applies, we use the particle distribution to find the centre of mass and iterate until convergence. We repeat the procedure using a smaller radius, $r = r_i$, where $r_i = r_{\text{sp}}/2^{1/2}$. We continue this method until $r_i = r_L$, where r_L is defined by the criterion $r_L > f_{\text{res}} > r_{L+1}$, or until reduction leads to an empty sphere.

(iii) We unify the spheres whose centres are within r_L of each other. The unification is performed by making a density weighted guess for a common centre of mass, and then iterating to find a centre of mass for the unified object by counting particles. The size of sphere used to determine the centre of mass is the smallest radius that will allow the new sphere to entirely contain both candidate halo spheres.

(iv) For each candidate halo centre we step out in radial shells of $1 h^{-1}$ kpc, counting enclosed particles, in order to find the outer radius of the halo: $R_h = \min(R_{\text{vir}}, R_t)$. The radius R_{vir} is the virial radius, and R_t is a “truncation” radius, defined as the radius ($< R_{\text{vir}}$) in which a rise in (spherical) density is detected ($d \log \rho / d \log r > 0$). This is our method for estimating when a different halo starts to overlap with the current halo and is important for haloes in crowded regions. We estimate the significance of a measured upturn using the Poisson noise associated with the number of particles in the radial bins considered. Only if the signal to noise of the upturn is larger than σ_{R_t} do we define a truncation radius. The value of σ_{R_t} is a free parameter. We use $\sigma_{R_t} = 1.5$. **

(v) Among the halo candidates for which we have found an R_{vir} , we discard those with $N_{\text{vir}} < N_p^{\text{min}}$, where N_{vir} is the number of particles within R_{vir} . Among the halo candidates for which we have found a rise in spherical density, we discard those which contain less than $N_{R_t}^{\text{min}}$ particles, where $N_{R_t}^{\text{min}} = N_p^{\text{min}}$ if $R_t > R_{\text{vir}}^{\text{min}}$, otherwise

$$N_{R_t}^{\text{min}} = N_p^{\text{min}} \left(\frac{R_t}{R_{\text{vir}}^{\text{min}}} \right). \quad (\text{B3})$$

** The choice was motivated by several tests using mock catalogues of haloes in clusters designed to determine how varying σ_{R_t} affects our ability to fit the density profiles of subhaloes. Although our results were not strongly dependent on this choice, we did obtain the best fits using $\sigma_{R_t} = 1.5$.

The above constraint follows from an extrapolation of the minimum mass halo using an isothermal profile $\rho(r) \propto 1/r^2$.

(vi) We model the density profile of each halo using the NFW form (Eq 1) and determine the best fit r_s and ρ_s values, which determine R_{vir} and M_{vir} . The fitting procedure uses logarithmically spaced radial bins from $\max(2f_{\text{res}}, 0.02 \times \min(R_{\text{vir}}, R_t))$ out to R_h . If any bins are empty we decrease the number of bins by one until all bins are full. If the number of bins is reduced below 3 we discard the halo as a local perturbation.

The fit takes into account the Poisson error in each bin due to the finite number of particles, and we obtain errors on the fit parameters (σ_{r_s} and σ_{ρ_s}) using the covariance matrix in the fit routine. The errors on the fit parameters can be translated easily into errors for R_{vir} ($\sigma_{R_{\text{vir}}}$) and the estimated NFW mass of each halo, M_{vir} (σ_M).

(vii) We unify haloes which overlap in R_s . Our criterion is met if two (or more) halo centres have R_s radii which overlap with each other while at the same time having velocities which allow them to be bound to the common system. If such a case occurs, then along with the individual halo NFW fits, we fit another NFW profile about the common centre of mass of the two combined haloes and decide whether the candidate-united-haloes are bound/unbound to the common NFW fit using the radial escape velocity determined using the common NFW profile (see below). If both haloes are bound we combine the two haloes into one, and keep the common fit for the characteristic parameters. If at least one is not bound, we do not combine the haloes.

An exception to this unifying criterion occurs if the fit errors on R_s are large ($\sigma_{R_s}/R_s > 1$), we replace $R_s \rightarrow \min(R_s, R_t)$. In addition if the R_s of a halo obeys $R_s > R_{\text{vir}}^{\text{min}}$ then we relax the strict combining of overlapping haloes. This case, which we refer to as the ‘‘cD’’ halo case, is discussed below (see (ix)).

(viii) For each halo, we remove all unbound particles before we obtain the final fits. We loop over all particles within the halo and declare a particle at a distance r from the centre of a halo to be unbound if its velocity relative to the centre of mass velocity of the halo obeys $v > \sqrt{2|\Phi_{\text{NFW}}(r)|}$, where the radial potential for NFW density profile is given by^{††}

$$\Phi_{\text{NFW}}(r) = -4\pi G\rho_s R_s^2 \left[\frac{\log(1+x)}{x} \right]. \quad (\text{B4})$$

After removal, we construct a new density profile and find new NFW fit parameters. The procedure is repeated until the number of unbound particles becomes $< 1\%$ of the bound particles or until $M_{\text{vir}}^{\text{NFW}} < M_{\text{halo}}^{\text{min}}$, in which case the halo is discarded.

An exception to this removal scheme occurs if two haloes lie within the virial radius of each other and the ratio of their masses are at least 0.75. We define haloes in this situation to be a ‘‘partner’’ pair. For each halo in this situation, we take not only its potential into account, but also that of its partner.

(ix) An interesting case of subhalo structure, which would otherwise be excluded from our finding algorithms, is that of

^{††} Note that this potential is *not* necessarily the physical gravitational potential at the halo location. For a subhalo, for example, the host background potential is *not* included.

one or more density peaks close to the centre of a large halo. We shall refer to these inner density peaks as cD cases. If a halo, after its unbound particles have been removed, obeys the following criteria, it is a candidate for containing cD haloes: a) the NFW fit has a standard GoF < 0.1 , b) the halo is a host of at least one subhalo, and c) the halo is ‘‘large’’, with $r_s > R_{\text{vir}}^{\text{min}}$.

We identify the potential centres of cD haloes by searching the bound particle distribution within r_s of each candidate cD halo using a CIC process on a fine grid ($r_{\text{sp1}} = \alpha f_{\text{res}}$). We discard all candidate density peaks with local densities less than the extrapolated minimum density (above the background density) within the core region of our smallest halo (see item (i)).

For each density maxima located farther than r_{sp1} from the centre of the candidate host halo, we find R_t and fit a NFW profile with iterative unbound particle removal. These are our cD haloes. cD haloes are discarded if their extrapolated virial mass is lower than our minimal mass halo.

Because we have a strict mass limit $M_{\text{vir}}^{\text{min}} = N_p^{\text{min}} \times m_p$, we expect our halo finder to be somewhat incomplete just above $M_{\text{vir}}^{\text{min}}$. We have also checked our completeness in two ways. First, we used a separate BDM halo finder that does not attempt to fit profiles and does not demand the unification of haloes within a specified radius. It does, however, unify haloes that have equal velocities within 15% as long as they have centres within $\sim 150 h^{-1} \text{kpc}$ (see Klypin & Holtzman 1997). This procedure allows a complete identification of DM haloes down to much lower particle numbers than our own. In order to check our results we have assigned to each halo in the catalog produced by the other finder a typical r_s given its mass, and checked the returned halo list for consistency against our catalogue from the same simulation box. For $N_{\text{particles}} \sim 150$, we estimate $\sim 80\%$ completeness and for $N_{\text{particles}} \sim 500$ we obtain $\geq 95\%$ completeness. A second, and almost identical completeness determination is obtained by carefully analyzing the roll-over in our observed mass function (Sigad et al. 1999). We attribute our incompleteness for small masses to our fitting procedure, and errors associated with this process.

APPENDIX C: REDUCING TF SCATTER

As discussed in §6, we find for distinct haloes a 1σ scatter at fixed M_{vir} of $\Delta V_{\text{max}}/V_{\text{max}} \simeq 0.12$, which is between 1.3 and 4 times the range of the reported intrinsic TF scatter. If these Λ CDM haloes are to host galaxies like those observed, this excessive scatter must be reduced. The translation of the halo virial mass into a disc luminosity, and of the original halo V_{max} into a final observed disc velocity, should somehow decrease the scatter. Following is a qualitative analysis of how this can come about in a natural way. The idea is that for a fixed halo mass and spin, a higher V_{max} should induce further gas contraction into smaller radii, and therefore higher gas density, star-formation rate and luminosity. This can be shown in a little more detail, as follows.

The size of the exponential disc, r_d , that forms by a dissipative contraction of gas inside a given dark-matter halo can be estimated under the adiabatic baryonic-infall approximation. We showed in §8 (see Equation 19) that r_d is a decreasing function of c_{vir} for haloes of a fixed virial mass and

spin, as long as the disc mass is a constant fraction of M_{vir} . For a typical case of a $V_{\text{vir}} = 200$ km/s halo, we demonstrated that, in the range encompassing 68% of c_{vir} for such haloes ($c_{\text{vir}}:9.2 \rightarrow 21.3$), the corresponding spread in disc sizes is $R_d : 4.0 \rightarrow 2.6 h^{-1}\text{kpc}$. Across this range, an effective power-law approximation would therefore be $r_d \propto c_{\text{vir}}^{-0.5}$. If (a) the gas density in the disc scales like $\rho \propto r_d^{-2}$, (b) the star formation rate obeys a typical Schmidt law, $\dot{\rho} \propto \rho^{1.5}$, and (c) the luminosity scales like $L \propto \dot{\rho} r_d^2$, then the luminosity at a given mass depends on c_{vir} as $L \propto r_d^{-1} \propto c_{\text{vir}}^{0.5}$. Since V_{max} (for a fixed V_{vir}) is also a monotonic function of c_{vir} (Eq. 6; the effective power-law approximation across the 68% range is $V_{\text{max}} \propto c_{\text{vir}}^{0.27}$), we have obtained a positive correlation between L/M_{vir} and the deviation of V_{max} from the median V_{max} at a given M_{vir} . Ignoring, for the moment, any difference between the V_{max} of the original halo and that of the disc, the obtained correlation would correspond to a reduced scatter in L by a factor larger than 2, as required. The effect of the spread in spins on the TF scatter is expected to be reduced for similar reasons, namely, because the luminosity and the maximum velocity are both expected to correlate with the spin in the same sense.

More detailed modelling, which takes into account how V_{max} changes as the baryons fall in, will be needed to test this hypothesis in detail.

REFERENCES

- Avila-Reese V., Firmani, C., Klypin, A., Kravtsov A.V., 1999, MNRAS, in press
- Barnes J., Efstathiou G., 1987, ApJ, 319, 575
- Bernstein G.M., Guhathakurta P., Raychaudhury S., Giovanelli R., Haynes M.P., Herter T., Vogt N.P. 1994, AJ, 107, 1962
- Blumenthal G. R., Faber S. F., Flores R., Primack J. R., 1986, ApJ, 301, 27
- Blumenthal G. R., Faber S. F., Primack J. R., Rees M. J., 1984, Nat, 311, 517
- Bothun, G.D., Schombert, J.M., Impey, C.D., Sprayberry, D., McGaugh, S.S., 1993, AJ, 106, 530
- Bryan G., Norman M., 1998, ApJ, 495, 80
- Bullock J. S., 1999, Ph.D. thesis, University of California, Santa Cruz
- Bullock J. S., Kolatt T. S., Sigad Y., Kravtsov A. V., Klypin A. A., Primack J. R., Dekel A., 1999a, in preparation
- Bullock J. S., Kollat T. S., Faber S. M., Primack J. R., & Dekel A. 1999b, in preparation
- Burkert, A., 1995, ApJ, 447, L25
- Craig M., 1997, Ph.D. thesis, University of California, Berkeley
- Dalcanton J. J., Spergel D. N., Summers F. J., 1997, ApJ, 482, 659
- Dressler A., 1980, ApJ, 236, 351
- Eisenstein D. J., Loeb A., 1996, ApJ, 459, 432
- Flores R., Primack J. R., Blumenthal G. R., Faber S. F., 1993, ApJ, 412, 443
- Ghigna S., Moore B., Governato F., Lake G., Quinn T., Stadel J., 1998, MNRAS, 300, 146
- Hockney R.W., Eastwood J.W. 1981, Computer simulations using particles (New York: McGraw-Hill)
- Jing Y., 1999, ApJ, Submitted, astro-ph/9901340
- Klypin A. A., Gottloeber S., Kravtsov A. V., Khokhlov A. M., 1999, ApJ, 516, 530
- Klypin A. A., Holtzman J., 1997, astro-ph/9712217
- Kolatt T. S., Bullock J. S., Sigad Y., Kravtsov A. V., Klypin A. A., Primack J. R., Dekel A., 1999b, in preparation
- Kolatt T. S. et al., 1999a, ApJL, accepted, astro-ph/9906104
- Kravtsov A. V., Klypin A. A., Bullock J. S., Primack J. R., 1998, ApJ, 502, 48 (KKBP)
- Kravtsov A. V., Klypin A. A., Khokhlov A. M., 1997, ApJS, 111, 73 (KKK97)
- Lacey C., Cole S., 1993 MNRAS, 262, 627
- Lowenthal et al., 1997, ApJ, 481, 673
- Mo, H.J., McGaugh, S.S., Bothun, G.D., 1994, MNRAS, 267, 129
- Mo H. J., Mao S., White S. D. M., 1998, MNRAS, 295, 319
- Mo H. J., Mao S., White S. D. M., 1999, MNRAS, 304, 175
- Moore B., Quinn T., Governato F., Stadel J., Lake G., 1999, MNRAS, submitted, astro-ph/9903164
- Navarro J. F. & Steinmetz M. S., 1999, ApJ, accepted, astro-ph/9908114
- Navarro J. F., 1998, ApJ, submitted, astro-ph/9807084
- Navarro J. F., Frenk C. S., White S. D. M., 1995, MNRAS, 275, 56 (NFW95)
- Navarro J. F., Frenk C. S., White S. D. M., 1996, ApJ, 462, 563 (NFW96)
- Navarro J. F., Frenk C. S., White S. D. M., 1997, ApJ, 490, 493 (NFW97)
- Okamoto T., Habe A., 1998, ApJ, accepted, astro-ph/9811362
- Peebles P. J. E., 1969, ApJ, 155, 393
- Peebles P. J. E., 1984, The Large-Scale Structure of the Universe (Princeton:Princeton Univ. Press)
- Postman M., Geller M. J., 1984, ApJ, 281, 95
- Press W. H., Schechter P., 1974, ApJ, 187, 425
- Primack J. R., Bullock J. S., Kravtsov A. V., Klypin A. A., 1998, Rutgers ‘‘Galaxy Dynamics’’ conference proc., astro-ph/9812241
- Sigad Y., Kolatt T. S., Bullock J. S., Kravtsov A. V., Klypin A. A., Primack J. R., Dekel A., 1999, in preparation
- Somerville R. S., Primack J. R., Faber S. M., 1999, MNRAS, accepted, astro-ph/9806228
- Steidel C. C., Gialalisco M., Dickinson M., Adelberger K. L., 1996, AJ, 112, 352
- Vogt N. P. et al., 1997, ApJ, 479, 121
- Warren M. S., Quinn P. J., Salmon J. K., Zurek W. H., 1992, ApJ, 399, 405
- Willick J.A., Courteau S., Faber S.M., Burnstein D., Dekel A., & Kolatt T., 1996, ApJ, 457, 460
- White S. D. M., Frenk C. S. , 1991, ApJ, 379, 52
- White S. D. M., Rees M. J., 1978, MNRAS, 183, 341